J|A|C|S
ARTICLES
Published on Web 11/13/2004

Porphyrin Boxes Constructed by Homochiral Self-Sorting Assembly: Optical Separation, Exciton Coupling, and Efficient Excitation Energy Migration

In-Wook Hwang,[†] Taisuke Kamada,[‡] Tae Kyu Ahn,[†] Dah Mee Ko,[†] Takeshi Nakamura,[‡] Akihiko Tsuda,[‡] Atsuhiro Osuka,*[,‡] and Dongho Kim*[,†]

Contribution from the Center for Ultrafast Optical Characteristics Control and Department of Chemistry, Yonsei University, Seoul 120-749, Korea, and Department of Chemistry, Graduate School of Science, Kyoto University, and CREST (Core Research for Evolutional Science and Technology) of the Japan Science and Technology Agency, Kyoto 606-8502, Japan

Received June 24, 2004; E-mail: osuka@kuchem.kyoto-u.ac.jp; dongho@yonsei.ac.kr

Abstract: *meso*-Pyridine-appended zinc(II) porphyrins **M*n*** and their *meso*−*meso*-linked dimers **D*n*** assemble spontaneously, in noncoordinating solvents such as $CHCl_3$, into tetrameric porphyrin squares **S*n*** and porphyrin boxes **B*n***, respectively. Interestingly, formation of **B*n*** from **D*n*** proceeds via homochiral self-sorting assembly, which has been verified by optical separations of **B1** and **B2**. Optically pure enantiomers of **B1** and **B2** display strong Cotton effects in the CD spectra, which reflect the length of the pyridyl arm, thus providing evidence for the exciton coupling between the noncovalent neighboring porphyrin rings. Excitation energy migration processes within **B*n*** have been investigated by steady-state and time-resolved spectroscopic methods in conjunction with polarization anisotropy measurements. Both the pump-power dependence on the femtosecond transient absorption and the transient absorption anisotropy decay profiles are directly associated with the excitation energy migration process within the **B*n*** boxes, where the exciton−exciton annihilation time and the polarization anisotropy rise time are well described in terms of the Förster-type incoherent energy hopping model by assuming a number of hopping sites of $N = 4$ and an exciton coherence length of $L = 2$. Consequently, the excitation energy hopping rates between the zinc(II) diporphyrin units have been estimated for **B1** $(48\ \text{ps})^{-1}$, **B2** $(98 \pm 3\ \text{ps})^{-1}$, and **B3** $(361 \pm 6\ \text{ps})^{-1}$. Overall, the self-assembled porphyrin boxes **B*n*** serve as a well-defined three-dimensional model for the light-harvesting complex.

Introduction

Currently, much effort has been directed toward unraveling the energy transport phenomena occurring in natural light-harvesting complexes.[1−3] At the same time, the mimicry of natural light-harvesting complexes has been continuously attempted by the covalent synthesis of various types of porphyrin or related pigment arrays with the goal of applying these arrays to artificial light-harvesting systems and molecular photonic devices.[4−11] The covalent approach has advantages of robust stability and precise control in the spatial arrangement and connecting spacer. The judicious choice of a spacer will allow fine control of electronic interactions between chromophores. However, as the size and complexity of these systems grow, the covalent strategy becomes increasingly inefficient and tedious.

Supramolecular chemistry, using a strategy of noncovalent self-assembly of molecular units, has been developed as a highly promising means for the construction of two- or three-dimensional architectures that have specific structures, proper-

[†] Yonsei University.
[‡] Kyoto University and CREST of the Japan Science and Technology Agency.

(1) van Oijen, A. M.; Ketelaars, M.; Köhler, J.; Aartsma, T. J.; Schmidt, J. *Science* **1999**, *285*, 400.
(2) (a) Sundström, V.; Pullerits, T.; van Grondelle, R. *J. Phys. Chem. B* **1999**, *103*, 2327. (b) Polivka, T.; Sundtröm, V. *Chem. Rev.* **2004**, *104*, 2021.
(3) van Grondelle, R.; Novoderezhkin, V. *Biochemistry* **2001**, *40*, 15057.
(4) Wasielewski, M. R. *Chem. Rev.* **1992**, *92*, 435.
(5) Gust, D.; Moore, T. A.; Moore, A. L. *Acc. Chem. Res.* **2001**, *34*, 40.
(6) Holten, D.; Bocian, D. F.; Lindsey, J. S. *Acc. Chem. Res.* **2002**, *35*, 57.
(7) Debreczeny, M. P.; Svec, W. A.; Marsh, E. M.; Wasielewski, M. R. *J. Am. Chem. Soc.* **1996**, *118*, 8174.
(8) Kodis, G.; Liddell, P. A.; de la Garza, L.; Clausen, P. C.; Lindsey, J. S.; Moore, A. L.; Moore, T. A.; Gust, D. *J. Phys. Chem. A* **2002**, *106*, 2036.
(9) (a) Kim, D.; Osuka, A. *J. Phys. Chem. A* **2003**, *107*, 8791. (b) Tsuda, A.; Osuka, A. *Science* **2001**, *293*, 79. (c) Cho, H. S.; Jeong, D. H.; Cho, S.; Kim, D.; Matsuzaki, Y.; Tanaka, K.; Tsuda, A.; Osuka, A. *J. Am. Chem. Soc.* **2002**, *124*, 14642. (d) Aratani, N.; Cho, H. S.; Ahn, T. K.; Cho, S.; Kim, D.; Sumi, H.; Osuka, A. *J. Am. Chem. Soc.* **2003**, *125*, 9668. (e) Cho, H. S.; Rhee, H.; Song, J. K.; Min, C.-K.; Takase, M.; Aratani, N.; Cho, S.; Osuka, A.; Joo, T.; Kim, D. *J. Am. Chem. Soc.* **2003**, *125*, 5849.
(10) (a) Choi, M.-S.; Yamazaki, T.; Yamazaki, I.; Aida, T. *Angew. Chem., Int. Ed.* **2004**, *43*, 150. (b) Choi, M.-S.; Aida, T.; Yamazaki, T.; Yamazaki, I. *Chem.—Eur. J.* **2002**, *8*, 2667. (c) Choi, M.-S.; Aida, T.; Luo, H.; Araki, Y.; Ito, O. *Angew. Chem., Int. Ed.* **2003**, *42*, 4060.
(11) (a) Officer, D. L.; Burrell, A. K.; Reid, D. C. W. *Chem. Commun.* **1996**, 1657. (b) Mak, C. C.; Bampos, N.; Sanders, J. K. M. *Angew. Chem., Int. Ed.* **1998**, *37*, 3020. (c) Solladie, N.; Gross, M.; Gisselbrecht, J.-P.; Sooambar, C. *Chem. Commun.* **2001**, 2206. (d) Biemans, H. A. M.; Rowan, A. E.; Verhoeven, A.; Vanoppen, P.; Latterini, L.; Foekema, J.; Schenning, A. P. H. J.; Meijer, E. W.; de Schryver, F. C.; Nolte, R. J. M. *J. Am. Chem. Soc.* **1998**, *120*, 11054. (e) Rucareanu, S.; Mongin, O.; Schuwey, A.; Hoyler, N.; Gossauer, A.; Amrein, W.; Hediger, H.-U. *J. Org. Chem.* **2001**, *66*, 4973. (f) Yeow, E. K. L.; Ghiggino, K. P.; Reek, J. N. H.; Crossley, M. J.; Bosman, A. W.; Schenning, A. P. H. J.; Meijer, E. W. *J. Phys. Chem. B* **2000**, *104*, 2596. (g) Taylor, P. L.; Wylie, A. P.; Huuskonen, J.; Anderson, H. L. *Angew. Chem., Int. Ed.* **1998**, *37*, 986.

ties, and functions.[12] Inspired by the noncovalent nature of natural photosynthetic systems, the self-assembly approach has been increasingly attempted in the mimicry of light-harvesting and charge separation systems.[13] Among these, the coordination interaction between zinc(II) porphyrin and pyridine is particularly useful for its easy manipulation, relatively large association, and a favorable tendency not to spoil the photo-excited-state dynamics of porphyrins.[14] Interesting examples so far reported include oligomeric conjugated porphyrin ladders developed by Anderson et al. that exhibit very large two-photon absorption cross-section,[15] energy-transfer and electron-transfer assemblies reported by Hunter et al.,[16] and giant porphyrin arrays and large porphyrin wheels as a model of light-harvesting antenna reported by Kobuke et al., where an imidazoyl substituent is used instead of a pyridyl substituent.[17] Spatial control of porphyrinic pigments is crucial in supramolecular design of artificial photosynthetic antennae, since it directly leads to control of the electronic interactions between chromophores. In this respect, a precise spatial control of porphyrin pigments with ample electronic interactions still remains challenging. For use as light-harvesting antennae, careful avoidance of energy sink that deactivates the excited state is another important requirement.

Molecular self-assembly can translate the covalent connectivity and molecular shape of the components into tertiary structure. In this context, the molecular component of a *meso*−*meso*-linked diporphyrin[18] is quite attractive because of its perpendicular conformation, which may lead to unique architectures. In addition, the two porphyrins in the component are strongly coupled mainly with Coulombic interaction but not π-conjugation.[18c] This encourages the possibility that properly self-assembled *meso*−*meso*-linked zinc(II) porphyrins serve as a model for light-harvesting antennae.

Here we report self-assembly behaviors of *meso*-pyridine-appended zinc(II) porphyrins **M1**−**M3** and their *meso*−*meso*-linked dimers **D1**−**D3** (Chart 1). In noncoordinating solvents, the monomeric porphyrins **M1**−**M3** assemble into porphyrin squares **S1**−**S3**, while the dimeric porphyrins **D1**−**D3** self-assemble into three-dimensional porphyrin boxes **B1**−**B3** (Chart 2). Self-assembly formation of porphyrin squares has been reported in other cases.[19,20] Among these, we reported the first X-ray crystal structure of **S1**.[19] Formation of the porphyrin box **B1** is of interest in view of its large association constant. In this study, we changed the size of the porphyrin box by inserting one and two phenyl groups between the porphyrin and pyridyl substituents. The three-dimensional zinc(II) porphyrin boxes

Chart 1. Structures of **D1**−**D3**, **D1H**−**D3H**, **T2H**, and **T2**

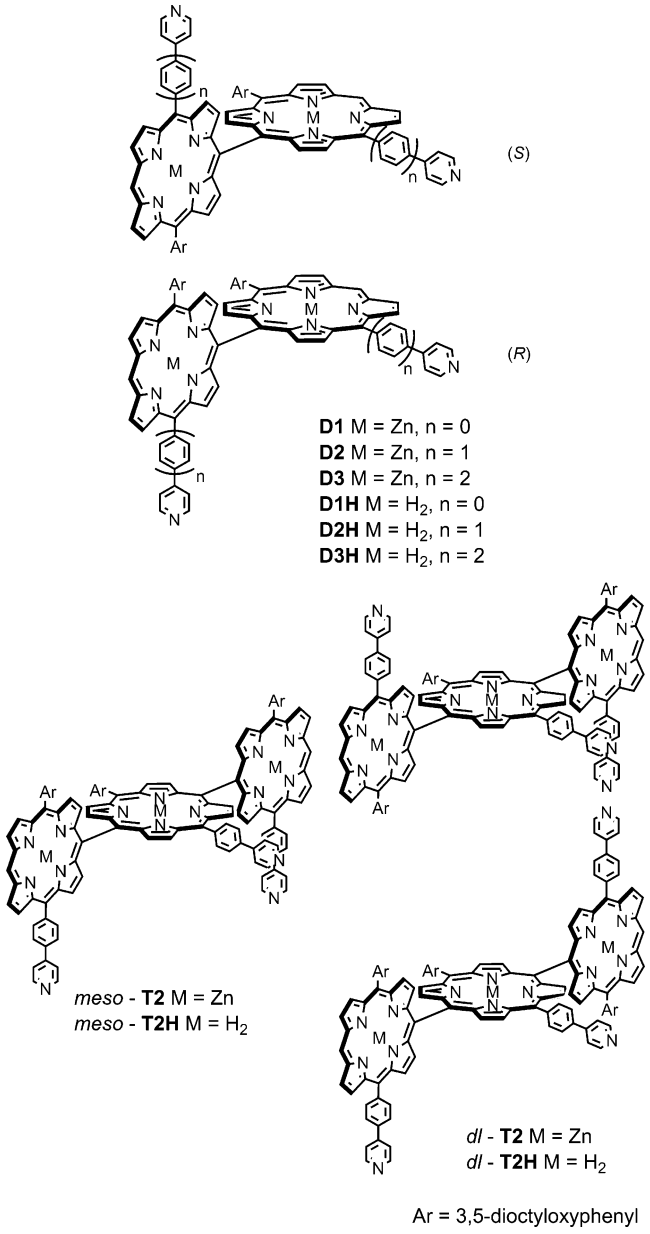

(12) (a) Lehn, J.-M. *Science* **2002**, *295*, 2400. (b) Hollingsworth, M. D. *Science* **2002**, *295*, 2410.

(13) (a) Hayashi, T.; Ogoshi, H. *Chem. Soc. Rev.* **1997**, *26*, 355. (b) Imamura, T.; Fukushima, K. *Coord. Chem. Rev.* **2000**, *198*, 133. (c) Wojaczynski, J.; Latos-Grazynski, L. *Coord. Chem. Rev.* **2000**, *204*, 113. (d) Chernook, A. V.; Rempel, U.; van Borczyskowski, C.; Shulga, A. M.; Zenkevich, E. I. *Chem. Phys. Lett.* **1996**, *254*, 229. (e) Flamigni, L.; Johnson, M. R. *New J. Chem.* **2001**, *25*, 1368. (f) Hartnell, R. D.; Arnold, D. P. *Organometallics* **2004**, *23*, 391.

(14) (a) Hunter, C. A.; Sanders, J. K. M.; Beddard, G. S.; Evans, S. *J. Chem. Soc., Chem. Commun.* **1989**, 1765. (b) Anderson, S.; Anderson, H. L.; Sanders, J. K. M. *Acc. Chem. Res.* **1993**, *26*, 469.

(15) (a) Wilson, G. S.; Anderson, H. L. *Chem. Commun.* **1999**, 1539. (b) Taylor, P. N.; Anderson, H. L. *J. Am. Chem. Soc.* **1999**, *121*, 11538. (c) Screen, T. E.; Thorne, J. R. G.; Denning, R. G.; Bucknall, D. G.; Anderson, H. L. *J. Am. Chem. Soc.* **2002**, *124*, 9712. (d) Screen, T. E.; Thorne, J. R. G.; Denning, R. G.; Bucknall, D. G.; Anderson, H. L. *J. Mater. Chem.* **2003**, *13*, 2796.

(16) (a) Hunter, C. A.; Hyde, R. K. *Angew. Chem., Int. Ed. Engl.* **1996**, *35*, 1936. (b) Haycock, R. A.; Yartsev, A.; Michelsen, U.; Sundström, V.; Hunter, C. A. *Angew. Chem., Int. Ed.* **2000**, *39*, 3616.

(17) (a) Ogawa, K.; Kobuke, Y. *Angew. Chem., Int. Ed.* **2000**, *39*, 4070. (b) Ogawa, K.; Zhang, T.; Yoshihara, K.; Kobuke, Y. *J. Am. Chem. Soc.* **2002**, *124*, 22. (c) Takahashi, R.; Kobuke, Y. *J. Am. Chem. Soc.* **2003**, *125*, 2372.

(18) (a) Osuka, A.; Shimidzu, H. *Angew. Chem., Int. Ed. Engl.* **1997**, *36*, 135. (b) Aratani, N.; Osuka, A.; Kim, Y. H.; Jeong, D. H.; Kim, D. *Angew. Chem., Int. Ed.* **2000**, *39*, 1458. (c) Kim, Y. H.; Jeong, D. H.; Kim, D.; Jeoung, S. C.; Cho, H. S.; Kim, S. K.; Aratani, N.; Osuka, A. *J. Am. Chem. Soc.* **2001**, *123*, 76.

(19) For a preliminary report of this work, see: Tsuda, A.; Nakamura, T.; Sakamoto, S.; Yamaguchi, K.; Osuka, A. *Angew. Chem., Int. Ed.* **2002**, *41*, 2817.

(20) (a) Fleischer, E. B.; Shachter, A. M. *Inorg. Chem.* **1991**, *30*, 3763. (b) Drain, C. M.; Lehn, J.-M. *J. Chem. Soc., Chem. Commun.* **1994**, 2313. (c) Chi, X.; Guerin, A. J.; Haycock, R. A.; Hunter, C. A.; Sarson, L. D. *J. Chem. Soc., Chem. Commun.* **1995**, 2567. (d) Funatsu, K.; Kimura, A.; Imamura, T.; Sasaki, Y. *Chem. Lett.* **1995**, *765*. (e) Fukushima, K.; Funatsu, K.; Ichimura, A.; Sasaki, Y.; Suzuki, M.; Fujihara, T.; Tsuge, K.; Imamura, T. *Inorg. Chem.* **2003**, *42*, 3187. (f) Stang, P. J.; Fan, J.; Olenyuk, B. *Chem. Commun.* **1997**, 1453. (g) Drain, C. M.; Nifiatis, F.; Vasenko, A.; Batteas, J. *Angew. Chem., Int. Ed.* **1998**, *37*, 2344. (h) Merlau, M.; Mejia, M. de P.; Nguyen, S. T.; Hupp, J. T. *Angew. Chem., Int. Ed.* **2001**, *40*, 4239. (i) Mines, G. A.; Tzeng, B.-C.; Stevenson, K.; Li, J.; Hupp, J. T. *Angew. Chem., Int. Ed.* **2002**, *41*, 154. (j) Iengo, E.; Zangrando, E.; Minatel, R.; Alessio, E. *J. Am. Chem. Soc.* **2002**, *124*, 1003. (k) Iengo, E.; Zangrando, E.; Alessio, E. *Eur. J. Inorg. Chem.* **2003**, 2371.

Chart 2. Structures of **S1**−**S3**, **B1**−**B3**, and **TB2**[a]

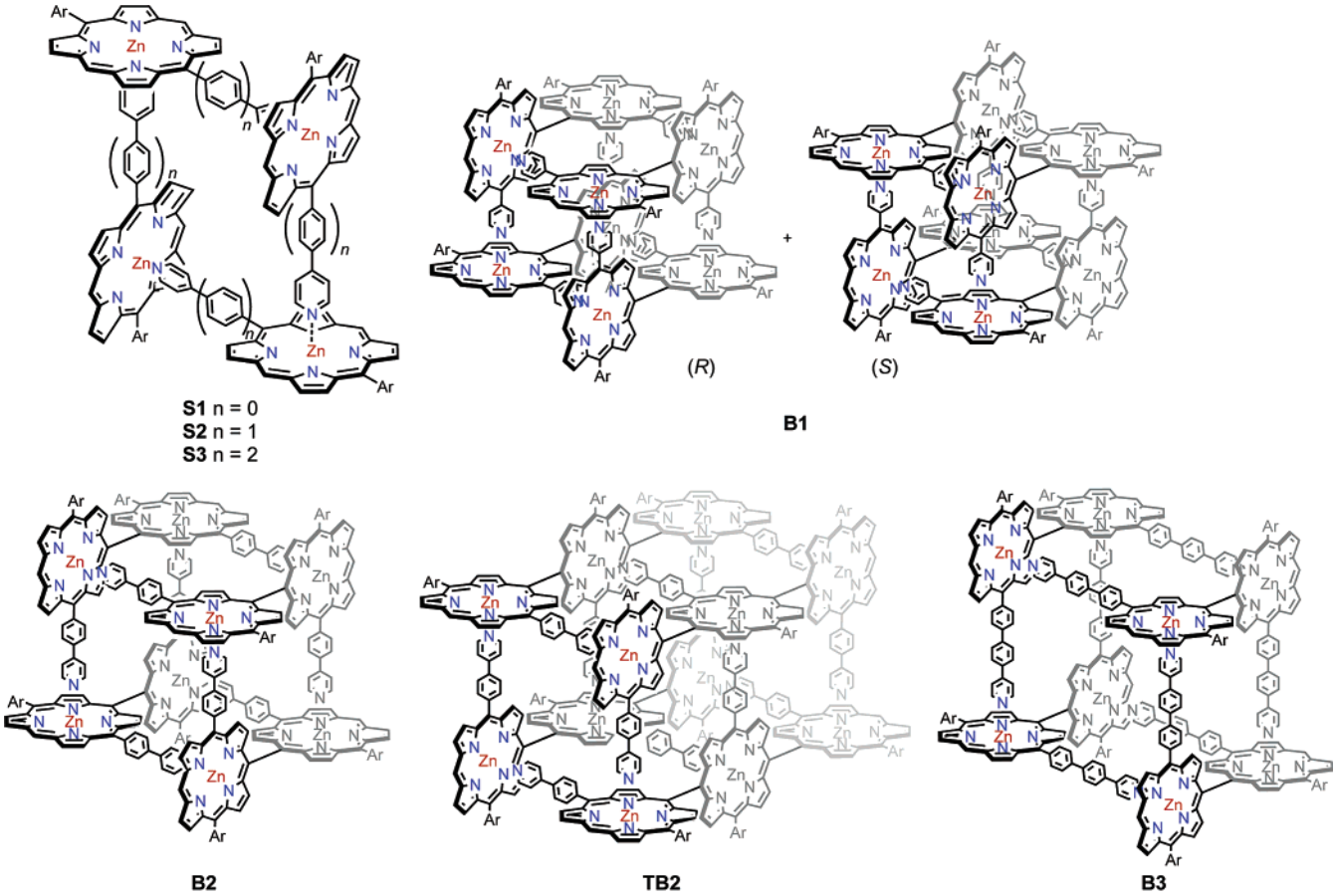

[a] Only structures of (*R*)-isomers are shown for **B2** and **B3**. Ar = 3,5-dioctyloxyphenyl.

B1−**B3** are well-defined discrete molecular entities that are pertinent for the investigations of excitonic interactions and excitation energy migration process. Thus, the excitation energy migration processes within **B1**−**B3** are comparatively investigated, using steady-state absorption and fluorescence measurements, the time-correlated single-photon counting technique (TCSPC), time-resolved fluorescence anisotropy measurements, and femtosecond transient absorption (TA) and transient absorption anisotropy (TAA) measurements. In the present study, **D*n*** molecules dissolved in strongly coordinating pyridine have been taken as a reference of five-coordinated free *meso*−*meso*-linked zinc(II) diporphyrin, and those dissolved in noncoordinative CH_2Cl_2 have been used for the measurements of **B*n***. As detailed later, the time-resolved fluorescence anisotropy decays have shown relatively slow rotational diffusion times, while the singlet−singlet exciton−exciton annihilation process in TA and the anisotropy decay profile in TAA measurements have identified and quantified the fast excitation energy hopping processes within **B1**−**B3**.

Results

Synthesis of Porphyrin Blocks. Synthetic routes to **M1**−**M3** are summarized in Scheme 1. Porphyrin **M1** was prepared from the reaction of 3,5-dioctyloxybenzaldehyde (**1**) and 4-formylpyridine (**2**) with 2,2′-dipyrrylmethane (**3**).[21] Similarly, 4-bromophenyl-appended and 4-bromobiphenyl-appended porphyrins **6** and **7** were prepared in 16% and 14% yields, respectively, using aldehydes **4** and **5** instead of **2**. Suzuki−Miyaura coupling of **6** and **7** with 4-pyridylboronic acid pinacol ester (**8**)[22] gave zinc(II) porphyrins **M2** and **M3** in 66% and 53% yields, respectively.

The *meso*−*meso* linkage in **D1** was previously made by Suzuki−Miyaura coupling of the appropriate partners, since Ag(I)-promoted dimerization of **M1** failed to give **D1** under the standard coupling conditions.[19] This time we found that Ag(I)-promoted coupling reaction of **M1** gave **D1** by refluxing the reaction mixture for a longer time. The Ag(I)-promoted coupling reaction of **M2** gave *meso*−*meso*-coupled diporphyrin **D2** and triporphyrin **T2** along with higher oligomers. Since the separation of these oligomers was practically impossible due to serious self-aggregation, these zinc(II) complexes were once demetalated to the corresponding free-base porphyrin oligomers, which were separated over preparative GPC to provide diporphyrin **D2H** and triporphyrin **T2H** in 32% and 14% yields, respectively. Similarly the Ag(I)-promoted coupling of **M3** gave **D3H** in 20% yield. Higher oligomers were formed but not isolated because of their very poor solubility.

Construction of Porphyrin Squares and Porphyrin Boxes. Construction of porphyrin square **S1** from **M1** was indicated by the characteristic ^{1}H NMR spectrum of **M1** in $CDCl_3$ at [**M1**]

(21) Ka, J.-W.; Lee, C.-H. *Tetrahedron Lett.* **2000**, *41*, 4609.
(22) Li, W.; Nelson, D. P.; Jensen, M. S.; Hoerrner, R. S.; Cai, D.; Larsen, R. D.; Reider, P. J. *J. Org. Chem.* **2002**, *67*, 5394.

Scheme 1. Synthesis of **M1**−**M3**

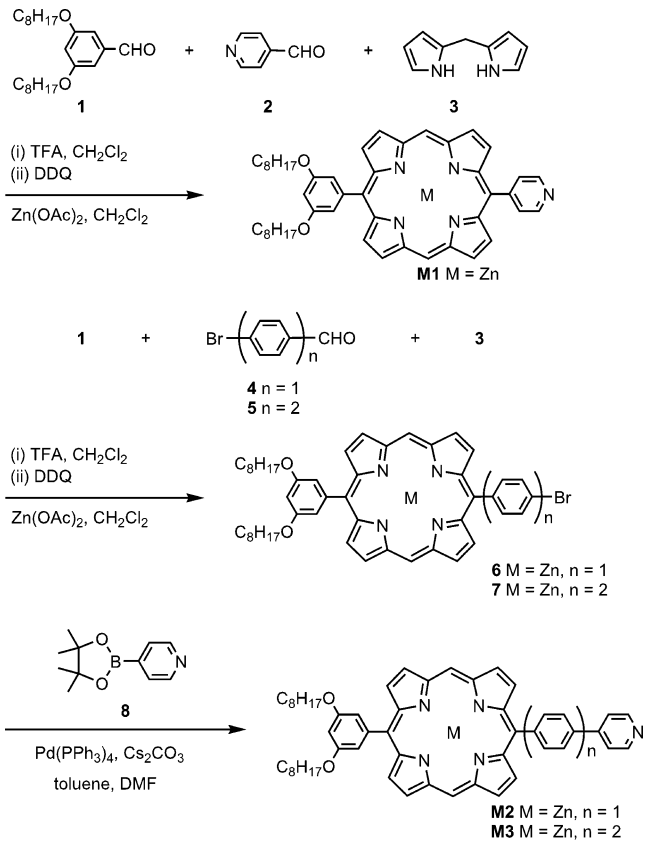

> 3 mM, which revealed large upfield shifts for the pyridyl protons. The X-ray crystal structure of **S1** showed a mutually coordinated square structure with nearly perpendicular dihedral angles (89.1° and 90.9°) between the neighboring porphyrins.[19] Almost quantitative formations of porphyrin squares **S2** and **S3** from **M2** and **M3** were both indicated by the characteristic ^{1}H NMR spectra in $CDCl_3$ ($\delta(H^\alpha) = 2.72$ ppm and $\delta(H^\beta) = 5.97$ ppm for **S2** and $\delta(H^\alpha) = 2.41$ ppm and $\delta(H^\beta) = 5.70$ ppm for **S3**) (Supporting Information). On the basis of concentration-dependent absorption changes, the association constants have been estimated to be 1.4×10^{15} for **S1**, 1.8×10^{12} for **S2**, and 7×10^{11} M^{-3} for **S3**, indicating dependence of the association constant on the length of the pyridyl side arm (Supporting Information).

Quantitative self-assembly of **D1** as its tetramer **B1** was confirmed by ^{1}H NMR spectroscopy in $CDCl_3$ and cold spray ionization mass spectroscopy (CSI-MS).[19] On the basis of the practical concentration independence of its fluorescence spectral shape (up to 1.0×10^{-8} M), the association constant of **B1** was estimated to be at least $>10^{25}$ M^{-3} in $CHCl_3$.[19]

Formation of porphyrin boxes **B2** and **B3** from **D2** and **D3** was similarly indicated by ^{1}H NMR spectra in $CDCl_3$ ($\delta(H^\alpha) = 2.78$ ppm and $\delta(H^\beta) = 6.05$ ppm for **B2** and $\delta(H^\alpha) = 2.79$ ppm and $\delta(H^\beta) = 5.93$ ppm for **B3**) (Supporting Information). Typically, ^{1}H NMR spectra of **D3H** and **D3** (**B3**) in $CDCl_3$ show the characteristic large upfield shifts for the pyridyl side chain of **D3**, supporting the formation of a discrete porphyrin box, **B3**.

The free-base triporphyrin **T2H** was separated into two diastereoisomers, **T2H-a** (fast eluting, 4%) and **T2H-b** (slow eluting, 10%), through a silica gel column. Zinc(II) insertion into **T2H-a** led to formation of insoluble and intractable polymeric material, while **T2H-b** gave a soluble discrete zinc complex that displayed a clear ^{1}H NMR spectrum. The H^α and H^β protons in the pyridyl substituents are observed at 2.82, 3.32, 6.09, and 6.28 ppm, hence suggesting the box formation. The association of the *meso*-isomer leads to formation of a discrete box assembly (**TB2**), while the association of the *dl*-isomer leads to an infinite linear array. On the basis of this consideration, **T2H-a** and **T2H-b** have been assigned, respectively, as *dl*-**T3H** and *meso*-**T3H** isomers.

Interestingly, in the GPC analyses with $CHCl_3$ as an eluent, **B1** exhibited a sharp elution band at a distinctly shorter retention time than that of **D1H**, which indicated the preservation of a discrete porphyrin box in the HPLC moving phase under highly diluted conditions. Similarly, the porphyrin boxes **B2** and **B3** preserve the tertiary structures in the GPC moving phase. The GPC eluting behaviors of **M2**, **D2**, and **T2** and their corresponding free-base counterparts **M2H**, **D2H**, and *meso*-**T2H** are compared (Supporting Information). The retention times of **D2** and **T2** are much shorter than those of **D2H** and *meso*-**T2H**, indicating the box formation. On the other hand, the retention time of **M2** is almost the same as that of **M2H**, indicating **M2** exists as a monomer in the GPC moving phase. The observed retention times reflect the molecular volumes of these self-assembled entities.

Steady-State Absorption, Fluorescence, and Fluorescence Excitation Anisotropy. Figure 1 shows the absorption and fluorescence spectra of (a) **D1**−**D3** in pyridine and (b) **B1**−**B3** in CH_2Cl_2. The peak positions are summarized in Table 1.

The absorption spectra of **D*n*** are characteristic of free *meso*−*meso*-linked zinc(II) diporphyrin, exhibiting Soret bands (S_0−S_2) that are split due to the exciton coupling between the porphyrin units.[18c,23] In the **D1**−**D3** series, the Soret bands are negligibly changed depending on the molecules, implying that the *meso*-substituted peripheral pyridyl substituents do not affect the exciton coupling between the porphyrin units. The fluorescence spectrum of **D1** is broad with peaks at 629 and 667 nm, which is also characteristic of five-coordinated free *meso*−*meso*-linked zinc(II) diporphyrins. The diporphyrins **D2** and **D3** display similar broad fluorescence spectra, while the relative intensity of the Q(0,0) fluorescence subband at short wavelength increases in going from **D1** to **D2** and **D3**. As for other free *meso*−*meso*-linked zinc(II) diporphyrins, the broad fluorescence spectra of **D1**−**D3** are interpreted in terms of a wide distribution in the dihedral angle between the two porphyrins, since changes in the dihedral angle influence the electronic interactions between the two porphyrins.

On the other hand, the absorption spectrum of **B1** (**D1** dissolved in CH_2Cl_2) exhibits a split Soret band ($\lambda_{max} = 426$ and 448 nm), but its splitting width is much less than that of free *meso*−*meso*-linked zinc(II) diporphyrins (e.g., the Soret band of **D1** in pyridine is split at 425 and 460 nm). This feature is entirely concentration independent even at very low concentration, ca. 10^{-7} M, which indicates a large association constant, at least 10^{21} M^{-3}. In contrast to those of the **D1**−**D3** series, the Soret bands of **B*n*** exhibit a systematic spectral change. While the high-energy Soret band remains at the same position, the low-energy Soret band shifts to the blue in the order **B3** < **B2**

(23) Cho, H. S.; Song, N. W.; Kim, Y. H.; Jeoung, S. C.; Hahn, S.; Kim, D.; Kim, S. K.; Yoshida, N.; Osuka, A. *J. Phys. Chem. A* **2000**, *104*, 3287.

Table 1. Band Maxima of Absorption and Fluorescence Spectra of **D*n*** and **B*n***[a]

		absorption (nm)					fluorescence (nm)		
sample	solvent	Soret (high)[b]	Soret (low)[b]	ΔE_{Soret}[c]	Q(1,0)	Q(0,0)	Q(0,0)	Q(0,1)	Φ_f[d]
D1	pyridine	424.9 (23535)	460.3 (21724)	(1811)	567	607	629	667	0.030
D2	pyridine	426.2 (23463)	460.4 (21720)	(1743)	568	609	633	668	0.015
D3	pyridine	426.6 (23441)	460.6 (21711)	(1730)	568	609	633	668	0.014
B1	CH_2Cl_2	426.3 (23457)	447.9 (22328)	(1129)	565	606	613	666	0.025
B2	CH_2Cl_2	426.3 (23457)	453.5 (22051)	(1406)	565	605	614	669	0.005
B3	CH_2Cl_2	426.6 (23441)	456.6 (21901)	(1540)	566	605	619	669	0.005

[a] The band position was determined by the Gaussian band-fitting process. [b] Values in parentheses are the absorption positions (cm^{-1}). [c] ΔE_{Soret} indicates the Soret band splitting energy (cm^{-1}). [d] Φ_f indicates the fluorescence quantum yield measured by excitation at 430 nm.

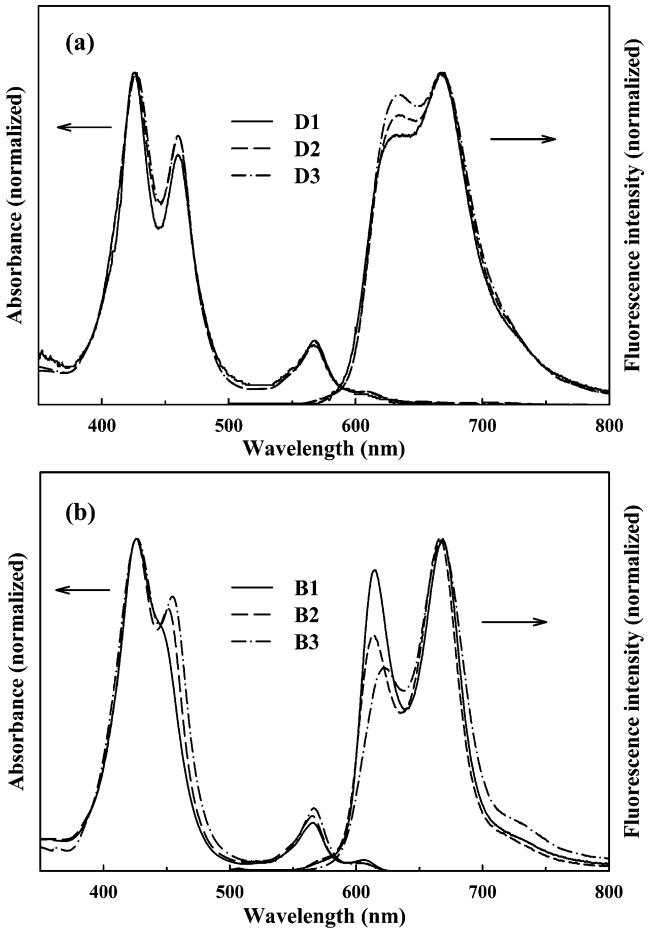

Figure 1. Steady-state absorption (left) and fluorescence (right) spectra of (a) **D*n*** and (b) **B*n***. The fluorescence spectra were obtained using an excitation wavelength of 430 nm, and the excitation wavelength dependence on the fluorescence spectra was negligible.

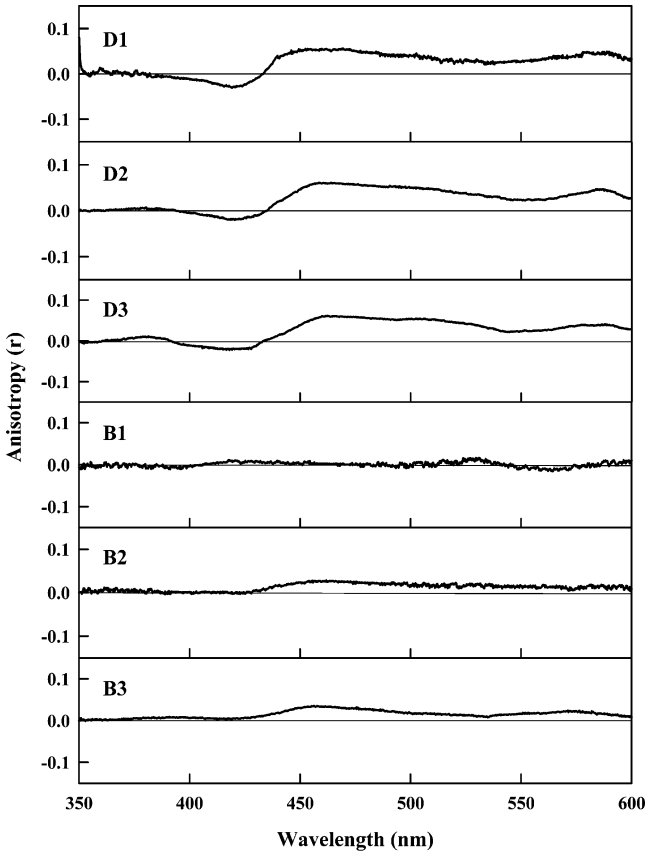

Figure 2. Steady-state fluorescence excitation anisotropy spectra of **D*n*** and **B*n***. The spectra were obtained using parallel and perpendicular orientations between excitation and emission polarizations, at a fixed emission wavelength of 610 nm.

< **B1**, resulting in a progressive decrease in the energy difference between the split Soret bands (ΔE_{soret}) (Figure 1b and Table 1). In contrast to the broad fluorescence spectra of **D1**−**D3**, the fluorescence spectrum of **B1** clearly shows a vibrational structure (λ_{max} = 613 and 666 nm). We interpreted the fluorescence spectrum of **B1** in terms of a small electronic interaction between the two porphyrins in the *meso*−*meso*-linked zinc(II) diporphyrin component, which is brought about as a *rigidification of its perpendicular conformation* upon box formation. In going from **B1** to **B2** and **B3**, the Q(0,0) fluorescence band is decreased in **B2** and is red-shifted in **B3**, while the Q(0,1) fluorescence subband at ~670 nm is not changed. In addition, the Stokes shifts are much less in **B1**−**B3** than those in **D1**−**D3**, probably reflecting more rigid conformations in the former. These characteristic fluorescence spectra of the boxes **B1**−**B3** are rather concentration independent up to 1.0×10^{-8} M, from which the association constants have been estimated to be at least 10^{24} M^{-3}. These large association constants have been interpreted in terms of effective cooperativity, where eight pyridine−zinc ion coordinations work simultaneously. Consistent with these results, the absorption spectrum of **TB2** exhibits Soret bands at 425.5 and 464.5 nm, while **T2** shows very split Soret bands at 424.5 and 480 nm (Supporting Information).

The steady-state fluorescence excitation anisotropy spectra were comparatively measured for **D1**−**D3** and **B1**−**B3** (Figure 2). This polarization anisotropy measurement is informative for the excitation energy migration process, because the energy migration between the same molecular units with different orientations provides a depolarization channel.[24] While **D1**−**D3** displayed common anisotropy profiles exhibiting negative anisotropy in the high-energy Soret band and positive anisotro-

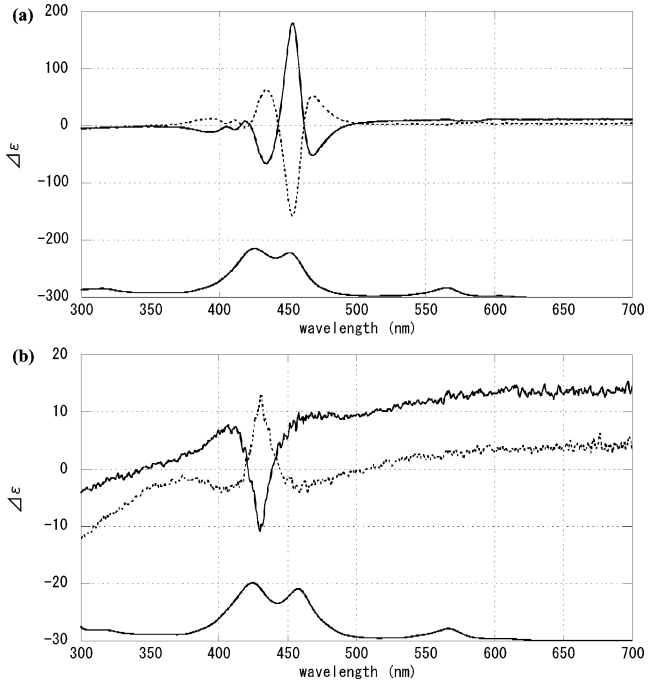

Figure 3. CD spectra of (a) **B2** taken in $CHCl_3$ and (b) **D2** taken in $CHCl_3$ and 20% pyridine. Absorption spectra taken under the same conditions are shown at the bottom of each panel. The solid line is for the first fraction, and the dotted line is for the second fraction.

pies in the low-energy Soret and Q bands,[18c,23] **B1**−**B3** showed distinctly different characteristics. First, the absolute anisotropy values over the entire absorption region are smaller in **B1**−**B3**. Second, the anisotropy values decreased in the order **B3** > **B2** > **B1**, indicating the efficient excitation energy migration over the **B*n*** boxes, whose efficiency is enhanced as the size of the porphyrin box decreases.

Optical Resolution of Chiral Porphyrin Boxes. Owing to the different *meso*-aryl substituents, **D1**−**D3** are all chiral, and hence, two enantiomers are present in equal abundance in solution, since a free rotation around the *meso*−*meso* linkage is severely prohibited. Accordingly, the porphyrin boxes **B1**−**B3** are chiral and are formed by *homochiral self-sorting assembly* of the respective (*R*)- and (*S*)-isomers of **D1**−**D3**. To prove this, we attempted the optical resolution of the porphyrin boxes against their noncovalent assembly nature. Actually the optical resolution of **B1** and **B2** has been accomplished with a chiral HPLC setup. Box **B2** showed two bands (fractions I and II) with comparable peak areas when chromatographed with hexane/CH_2Cl_2 (62/38) as eluent (Supporting Information). The two fractions were separated, both of which were found to be identical to the original **B2** in terms of the absorption and fluorescence spectra, while the circular dichroism (CD) spectra were perfect mirror images of each other (Figure 3a). Box **B1** was separated similarly, and the CD spectra were also measured (Supporting Information). In the case of **B2**, fraction I exhibited Cotton effects, negative at 469 nm, positive at 454 nm, and negative at 435 nm, and fraction II exhibited reverse Cotton effects at the same positions (Figure 3a). Addition of pyridine to a solution of chiral **B2** led to dissociation into **D2** fragments as revealed by the absorption changes. The pyridine-induced dissociation process was followed more clearly from the CD spectral changes, where the Cotton effect was significantly attenuated, less than one-tenth compared with those of **B2**. Dissociated fraction I exhibited only the negative Cotton effect at the high-energy Soret band (430 nm), and dissociated fraction II exhibited the reversed Cotton effect (Figure 3b). The CD spectra of optically separated **B1** are similar to those of **B2**, but the intensity at 450 nm is roughly doubled (Supporting Information). The CD spectra of **D1** are also similar to those of **D2**.

(24) (a) Yatskou, M. M.; Koehorst, R. B. M.; van Hoek, A.; Donker, H.; Schaafsma, T. J.; Gobets, B.; van Stokkum, I.; van Grondelle, R. *J. Phys. Chem. A* **2001**, *105*, 11432. (b) Yatskou, M. M.; Donker, H.; Novikov, E. G.; Koehorst, R. B. M.; van Hoek, A.; Apanasovich, V. V.; Schaafsma, T. J. *J. Phys. Chem. A* **2001**, *105*, 9498.

Table 2. Fitted Fluorescence Lifetimes and Anisotropy Decay Parameters of **D*n*** and **B*n***[a]

sample	solvent	fluorescence lifetime τ[b] (ns)	anisotropy decay parameters[c] r_0	Φ (ns)
D1	pyridine	1.70 ± 0.02	−0.046 ± 0.001	1.01 ± 0.24
D2	pyridine	1.79 ± 0.01	−0.061 ± 0.001	1.39 ± 0.40
D3	pyridine	1.83 ± 0.01	−0.053 ± 0.003	1.73 ± 0.50
B1	CH_2Cl_2	1.61 ± 0.02	−0.029 ± 0.001	4.69 ± 0.41
B2	CH_2Cl_2	1.67 ± 0.01	−0.030 ± 0.001	5.91 ± 0.61
B3	CH_2Cl_2	1.75 ± 0.02	−0.034 ± 0.002	9.30 ± 0.91

[a] An excitation wavelength of 420 nm was applied to all experiments. The fluorescence lifetimes were obtained by averaging the fitted single fluorescence lifetimes at several emission wavelengths. [b] Using the relation $I(t) = A_1 \exp(-t/\tau)$, where $I(t)$ is the time-dependent fluorescence intensity, A the amplitude, and τ the fitted fluorescence lifetime. The χ^2 values of the fittings were maintained as ∼1.0−1.5. [c] Using the relation $r(t) = r_0 \exp(-t/\Phi)$, where $r(t)$ is the time-dependent fluorescence anisotropy [$r(t) = (I_{\parallel}(t) - GI_{\perp}(t))/(I_{\parallel}(t) + 2GI_{\perp}(t)]$ and Φ the fitted rotational rise time.

Fluorescence Lifetime and Fluorescence Anisotropy Decay. The time-resolved fluorescence decays of **D*n*** and **B*n*** were measured (Supporting Information), and their fitted fluorescence lifetimes are tabulated in Table 2. The fluorescence decay becomes slightly faster in going from **D*n*** to **B*n***, and decreases in the order **D3** > **D2** > **D1**, as well as **B3** > **B2** > **B1** (see the τ values in Table 2). The τ value, however, did not reflect the energy migration process within **B*n***, because its time scale (∼1.6−1.8 ns) was considerably slow in view of the close proximity intermolecular coordination geometry of **B*n***. The fluorescence lifetimes come from the different S_1-state lifetimes of the porphyrin units. The analogous S_1-state lifetimes reflect an avoidance of energy sink in the **B*n*** boxes.

The fluorescence anisotropy decays of **D*n*** and **B*n*** were measured, where the excitation of the high-energy Soret band (λ_{ex} = 420 nm) was employed (Supporting Information). The fitted decay parameters are also tabulated in Table 2. The fluorescence anisotropy decay time constant (Φ) gradually increased in the order **D1** (1.0 ns) < **D2** (1.4 ns) < **D3** (1.7 ns), jumped to a level of 4.7 ns in **B1**, and further increased in **B2** (5.9 ns) and **B3** (9.3 ns), reflecting an increasing molecular volume of the box structure in this order. Therefore, the Φ values have been interpreted to originate from the rotational diffusion motion in solution. The fluorescence anisotropy decays consistently revealed negative amplitudes in agreement with the negative anisotropies at the high-energy Soret bands of the steady-state excitation anisotropy spectra (Figure 2). The excitation of the high-energy Soret band is known to induce a coherent energy hopping within a *meso*−*meso*-linked zinc(II) diporphyrin, which gives rise to a negative fluorescence anisotropy.[18c,23] Because this energy hopping proceeds on the time scale of <200 fs, it cannot be probed by the TCSPC system.[23] Finally, the fluorescence excitation anisotropy decays

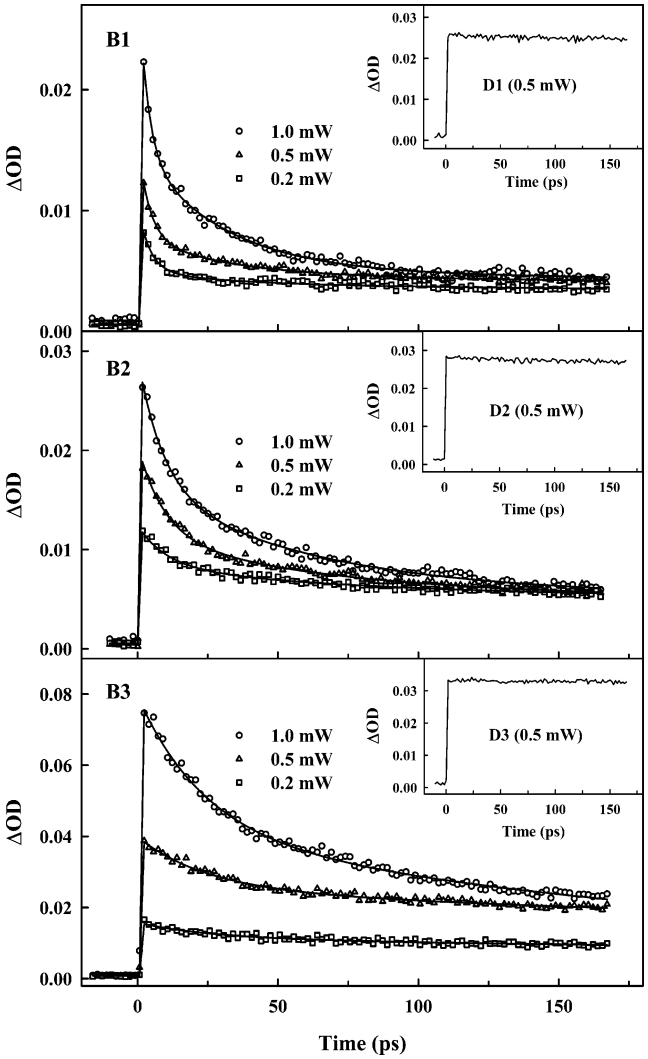

Figure 4. Transient absorption decay profiles of **B*n*** that include pump-power dependence. The transient absorption decay profiles of **D*n*** are shown as insets in the upper right corner of each panel. In the experiments, the pump and probe wavelengths are 570 and 490 nm, which are the Q band excitation and induced absorption probe.

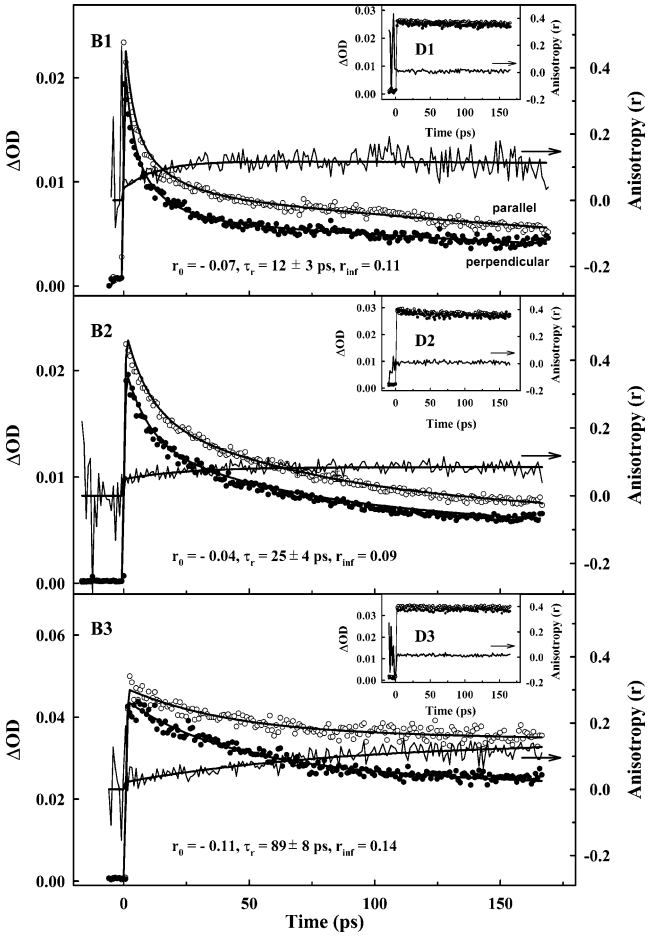

Figure 5. Transient absorption anisotropy decay profiles of **B*n***. The transient absorption decays for parallel and perpendicular orientations between pump and probe polarizations are included, and the fitted anisotropy decay parameters are listed at the bottom of each panel. The transient absorption anisotropy decay profiles of **D*n*** are shown as insets in the upper right corner of each panel. The pump and probe wavelengths were 570 and 490 nm, respectively.

revealed the excitation energy migration within **B*n***. The initial r_0 value of the fluorescence anisotropy decay became smaller in going from **D*n*** (~ -0.05) to **B*n*** (~ -0.03), indicating the presence of additional depolarization channels in **B*n***.

Femtosecond Transient Absorption and Transient Absorption Anisotropy. To investigate the fast excitation energy migration processes within **B*n***, both TA including pump-power dependence and TAA decays were measured (Figures 4 and 5), where the Q band excitation, i.e., $\lambda_{pump} = 570$ nm, was employed to avoid the involvement of S_2-S_1 relaxation.[25] The TA and TAA decays of **D*n*** were also measured as references (insets of Figures 4 and 5). **D*n*** revealed slow TA decays that are in agreement with the S_1-state lifetimes ($\sim$1.6−1.8 ns) found in the TCSPC measurements, and concomitantly did not show any anisotropy decay profiles in the time region of tens of picoseconds (insets of Figures 4 and 5). On the other hand, **B*n*** showed relatively fast TA decays along with anisotropy rises in the same time region, indicating fast depolarization processes. The exponential fittings for the TA decays of **B*n*** were performed using three decay components (τ_1, τ_2, and τ_3), where the slowest decay components τ_3 were fixed as the τ values in the TCSPC measurements (Table 3). The TA decays of **B*n*** were interestingly dependent upon both the pump power and the molecule. When the pump power was increased, the relative contributions of the fast τ_1 and τ_2 components were enhanced, as compared to that of τ_3. In addition, both τ_1 and τ_2 values systematically increased in the order **B1** < **B2** < **B3** (Table 3). The pump-power dependence on the decay is indicative of an exciton−exciton annihilation process, because the intense excitation or high density of photons generates two or more excitons in one assembly unit, and then the recombination between the excitons gives rise to a fast deactivation process.[25,26] Figure 4 indicates that the exciton−exciton annihilation process of **B*n*** is due to the exciton−exciton recombination between *meso*−*meso*-linked zinc(II) diporphyrins rather than zinc(II) porphyrin monomers, because this process does not occur in **D*n*** and becomes slower as the distance between the *meso*−

(25) Bradforth, S. E.; Jimenez, R.; van Mourik, F.; van Grondelle, R.; Fleming, G. R. *J. Phys. Chem.* **1995**, *99*, 16179.

(26) (a) Trinkunas, G.; Herek, J. L.; Polívka, T.; Sundström, V.; Pullerits, T. *Phys. Rev. Lett.* **2001**, *86*, 4167. (b) Trinkunas, G. *J. Lumin.* **2003**, *102*, 532. (c) Brüggemann, B.; May, V. *J. Chem. Phys.* **2004**, *120*, 2325. (d) Müller, M. G.; Hucke, M.; Reus, M.; Holzwarth, A. R. *J. Phys. Chem.* **1996**, *100*, 9537. (e) Brüggemann, B.; Herek, J. L.; Sundström, V.; Pullerits, T.; May, V. *J. Phys. Chem. B* **2001**, *105*, 11391.

Table 3. Transient Absorption Decay Parameters for **B*n*** Depending on the Pump Power[a]

pump power (mW)	fitted decay times[b] (ps)		
	τ_1	τ_2	τ_3
	Sample **B1**		
1.0	3 (44%)	30 (40%)	1610 (16%)
0.5	4 (46%)	30 (24%)	1610 (30%)
0.2	4 (48%)	30 (14%)	1610 (38%)
	Sample **B2**		
1.0	9 (42%)	57 (39%)	1670 (19%)
0.5	9 (42%)	60 (29%)	1670 (29%)
0.2	10 (31%)	59 (22%)	1670 (47%)
	Sample **B3**		
1.0	24 (48%)	230 (47%)	1750 (5%)
0.5	25 (37%)	228 (19%)	1750 (44%)
0.2	26 (30%)	228 (16%)	1750 (54%)

[a] The pump and probe wavelengths are 570 and 490 nm, respectively. [b] Using the relation $\Delta OD(t) = A_1 \exp(-t/\tau_1) + A_2 \exp(-t/\tau_2) + A_3 \exp(-t/\tau_3)$, where $\Delta OD(t)$ is the transient absorption intensity, A the amplitude (noted in parentheses as the normalized percentage, i.e., $[A_i/(A_1 + A_2 + A_3)] \times 100$), and τ the fitted decay time.

meso-linked zinc(II) diporphyrins increases in going from **B1** to **B2** and **B3**.

The TAA decays of **B*n*** were fitted using one rising component, i.e., 12 ps for **B1**, 25 ps for **B2**, and 89 ps for **B3** (Figure 5, inset). Increasing TAA rising time in the order **B1** < **B2** < **B3** indicates that not energy hopping within a *meso*−*meso*-linked zinc(II) diporphyrin but energy transfer between neighboring *meso*−*meso*-linked zinc(II) diporphyrins is responsible for this anisotropic rise. Here we note that the TAA of **B*n*** showed a single-exponential rising component, τ_r, even though the TA of **B*n*** revealed the two exciton−exciton annihilation components τ_1 and τ_2. The discrepancy between the exciton−exciton annihilation and the anisotropy depolarization, however, has often been found in other multichromophoric systems such as LH1 and LH2.[26] In a multichromophoric system, neither exciton−exciton annihilation nor anisotropy depolarization time is directly ascribed to the excitation energy hopping time, because they do not occur in a donor−acceptor pair. The energy hopping time can only be theoretically obtained by modeling the process.

It is noteworthy that **B*n*** displayed an anisotropy rise in the TAA measurement, which converges to ~0.1 at $t = \infty$, whereas **D*n*** showed constant anisotropy of $r_0 = r_\infty \approx 0$, in the time region of tens of picoseconds. Without rotational diffusion motion, the *meso*−*meso*-linked zinc(II) diporphryin has $r_\infty \approx 0$, because of its rodlike structure, and the zinc(II) porphyrin monomer has $r_\infty \approx 0.1$, because of its disklike structure.[25] Therefore, the TAA rise and $r_\infty \approx 0.1$ of **B*n*** imply that the excitation energy hopping process among the *meso*−*meso*-linked zinc(II) diporphryins leads to an alteration of molecular polarization from dimeric character to monomeric character.

To investigate the faster depolarization process within **D*n*** and **B*n***, the TAA measurements were performed in the time region of hundreds of femtoseconds (Supporting Information). The anisotropy decays consistently have decay times of <200 fs. In addition, the decay time becomes shorter in going from **D*n*** to **B*n***, as box formation occurs, where a more detailed description of the decay time is not applicable, because of the broad pump pulse (~150 fs). According to our previous report on the orthogonally linked zinc(II) porphyrin array, the coherent excitation energy hopping between the covalently linked porphyrin monomer units proceeds on this time scale (<200 fs).[18c,23]

Discussion

One of the key requirements for molecular design of photosynthetic models is a precise control of electronic interaction between porphyrin-like chromophores, since the electronic interaction is a key parameter in determining excitation energy transfer and electron transfer. This control is often very difficult in noncovalent assemblies, because of low chemical stability and ambiguous spatial arrangement. This stands in sharp contrast to strictly arranged chromophore arrays in natural antenna systems.

Zinc(II) insertion into *meso*-pyridyl-appended porphyrins and *meso*-pyridyl-appended *meso*−*meso*-linked diporphyrins drives the formation of porphyrin squares and boxes, respectively. Interestingly, box formation is accompanied by rigidification of the perpendicular conformation of *meso*−*meso*-linked diporphyrin, leading to very precise fixation of the spatial arrangement and hence the electronic coupling among porphyrins. While the association constant of porphyrin square **S*n*** depends on the length of the pyridyl arms, box formation proceeds with an exceptionally large association constant through simultaneous eight-point cooperative coordination, which is practically not affected by the presence of one or two 1,4-phenylene spaces between the porphyrin *meso*-position and 4-pyridyl group. Owing to the large association constants, **B*n*** behave like a covalently linked single chemical entity in noncoordinating solvents, which allows for the various steady-state and ultrafast measurements as well as the optical separation of **B1** and **B2**.

The porphyrin boxes **B1**−**B3** are formed via a homochiral self-sorting assembly process of **D1**−**D3**, respectively. These processes are aided by the dynamic nature of pyridine coordination toward zinc(II) porphyrin. Among many possible assembly routes, the homochiral self-sorting process leads to a discrete box, while the regularly alternate assembly of different enantiomers of **D*n*** leads to a linear infinite polymer network, and nonspecific assembly gives rise to ill-defined oligomers or polymers. The preferential formation of **B*n*** may be understood in terms of a favorable entropic gain toward other assembly processes.

Similar to other free *meso*−*meso*-linked zinc(II) diporphyrins, **D*n*** display split Soret bands due to exciton coupling.[18c,23] The Soret band of zinc(II) porphyrin monomer has two perpendicular transition dipole moments, $\mathbf{B}_x$ and $\mathbf{B}_y$, that are degenerate in a simple monomer (Scheme 2, left). In a *meso*−*meso*-linked zinc(II) diporphyrin, however, parallel $\mathbf{B}_z$ dipole moments couple effectively, whereas other dipole interactions should be virtually zero because of an averaged perpendicular conformation (Scheme 2, middle). Thus, the Soret bands of **D*n*** are split into a red-shifted $\mathbf{B}_z$ component and unperturbed $\mathbf{B}_x$ and $\mathbf{B}_y$ components. It is known that the dihedral angle is not strictly fixed at 90° but has a wide distribution of 90 ± 20°. This has been taken as a cause of the broad Soret band of *meso*−*meso*-linked zinc(II) diporphyrins. The electronic interaction should be a minimum at exactly 90° and increase upon a decrease in the dihedral angle. This was indeed confirmed by the examination of a series of permanently distorted 1,ω-dioxylmethylene-strapped *meso*−*meso*-linked zinc(II) diporphyrins[27] with dihedral

Scheme 2. Exciton Coupling in the Monomer, *meso*−*meso*-Linked Diporphyrin, and Porphyrin Box

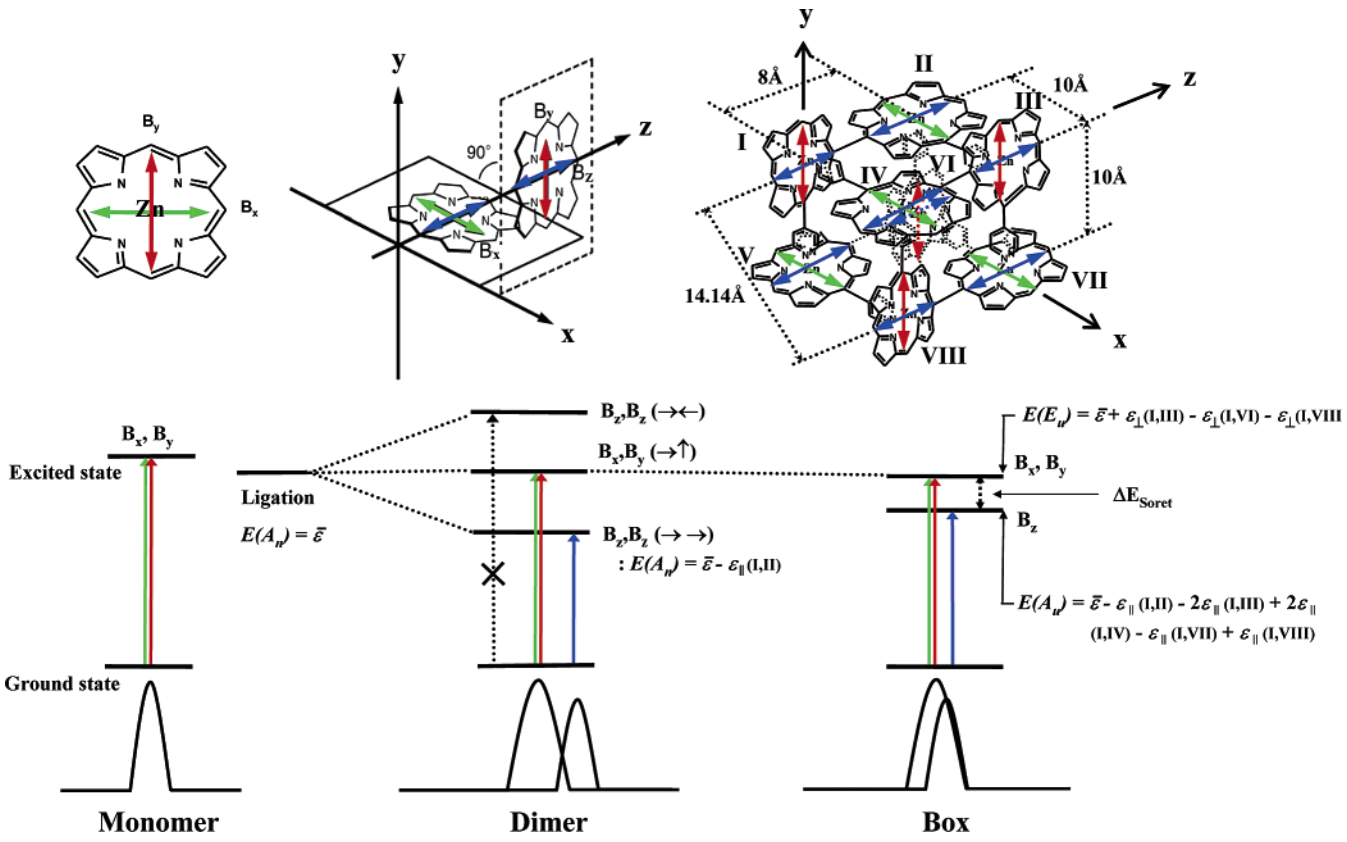

angles of less than 90° and was used as a switching excitation-energy-transfer component.[28] In this context, it is interesting to note that the boxes **B1**−**B3** exhibit common features of a small Soret band splitting and fluorescence spectrum with distinct vibrational structure, which indicate the attenuation of the electronic interaction within a *meso*−*meso*-linked zinc(II) diporphyrin in comparison to those in normal *meso*−*meso*-linked zinc(II) diporphyrins. We interpreted this attenuation in terms of the rigidification of a strictly perpendicular conformation of *meso*−*meso*-linked zinc(II) diporphyrin as a result of simultaneous multipoint coordinative interactions.

The CD spectra of optically active **D1**, **B1**, **D2**, and **B2** are quite informative on the orientations and mutual interactions of the transition dipole moments. The CD spectra of optically pure **D1** and **D2** exhibit weak bisignate exciton coupling at the high-energy Soret band. This Cotton effect can be considered to stem from the dipole coupling of $\mathbf{B}_x$ and $\mathbf{B}_y$, which are designated in Scheme 3, left, reflecting different *meso*-aryl substituents (3,5-dioctyloxyphenyl versus 4-pyridyl or 4-pyridylphenyl). The relatively small CD intensity can be related to a small different chiral environment caused by these different substituents. According to the empirical exciton chirality methods and related studies,[29,30] the first eluting isomer with a negative Cotton effect has been assigned as (*R*)-**D***n*, which has a counterclockwise arrangement of appended pyridyl substituents. The Cotton effects are remarkably very enhanced in **B1** and **B2** at both the high- and low-energy Soret bands. In the case of fraction I of **B2**, the first Cotton effect at 469 nm is negative and the second one at 454 nm is positive, thus indicating a counterclockwise arrangement of the transition dipole moments involved. Among many complicated exciton coupling interactions, these strong Cotton effects of **B2** have been assigned due to the coupling of coupled dipole moments ($\mathbf{B}_z + \mathbf{B}_z$) with perpendicularly arranged $\mathbf{B}_x$ or $\mathbf{B}_y$ in the neighboring diporphyrins in the porphyrin box formed from (*R*)-**D2**. As shown in Scheme 3, the coupled dipole moments ($\mathbf{B}_z + \mathbf{B}_z$) in the diporphyrin unit (III and IV) can interact strongly with $\mathbf{B}_y$(I) and $\mathbf{B}_x$(VII) and weakly with $\mathbf{B}_x$(V) and $\mathbf{B}_y$(VI) but cannot interact with $\mathbf{B}_z$(I), $\mathbf{B}_x$(II), $\mathbf{B}_z$(II), $\mathbf{B}_z$(V), $\mathbf{B}_z$(VI), $\mathbf{B}_z$(VII), $\mathbf{B}_y$(VIII), or $\mathbf{B}_z$(VIII) due to the coplanar arrangements. Here it is noted that the strongest interactions are apparently for the coupling of ($\mathbf{B}_z + \mathbf{B}_z$)(III, IV) with $\mathbf{B}_y$(I) and $\mathbf{B}_x$(VII), and thus, the spatial arrangements of these dipole moments are both interpreted to be counterclockwise. This interpretation has been supported by the CD spectra of **B1**, in which the corresponding Cotton effects are increased by a factor of 2, since **B1** has a shorter distance between the dipole moments that are responsible for the Cotton effects.

To explain the blue shift in the low-energy Soret band of **B***n* (Figure 1b, left), the following excitonic dipole coupling scheme

(27) (a) Yoshida, N. Osuka, A. *Org. Lett.* **2000**, *2*, 2963. (b) Yoshida, N.; Ishizuka, T.; Osuka, A.; Jeong, D. H.; Cho, H. S.; Kim, D.; Matsuzaki, Y.; Nogami, A.; Tanaka, K. *Chem.*−*Eur. J.* **2003**, *9*, 58.

(28) Shinmori, H.; Ahn, T. K.; Cho, H. S. Kim, D.; Yoshida, N.; Osuka, A. *Angew. Chem., Int. Ed.* **2003**, *42*, 2754.

(29) (a) Nakanishi, K.; Berova, N. In *Circular Dichroism: Principles and Applications*; Nakanish, K., Berova, N., Woody, R. W., Eds.; VCH Publishers Inc.: New York, 1994; p 361. (b) Mason, S. F. *Molecular Optical Activity and the Chiral Discriminations*; Cambridge University Press: Cambridge, 1982. (c) Harada, N.; Nakanishi, K. *Acc. Chem. Res.* **1972**, *5*, 257.

(30) (a) Kurtan, T.; Nesnas, N.; Li, Y.-Q.; Huang, X.; Nakanishi, K. Berova, N. *J. Am. Chem. Soc.* **2001**, *123*, 5962. (b) Pescitelli, G.; Gabriel, S.; Wang, Y. K.; Fleischhauer, J.; Woody, R. W.; Berova, N. *J. Am. Chem. Soc.* **2003**, *125*, 7613. (c) Borovkov, V. V.; Lintuluoto, J. M.; Inoue, Y. *J. Am. Chem. Soc.* **2001**, *123*, 2979.

Scheme 3. Structures of (*R*)-**D*n*** and (*R*)-**B*n***[a]

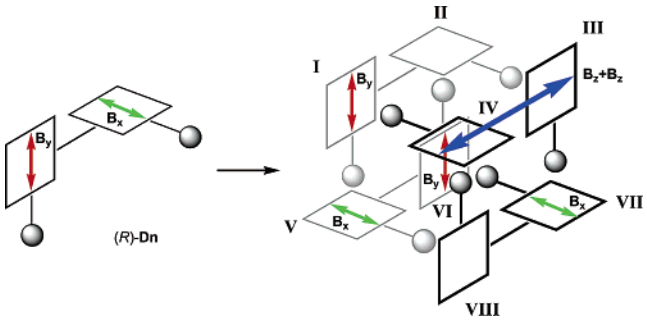

[a] In (*R*)-**B*n***, coupled dipole moments ($\mathbf{B}_z + \mathbf{B}_z$) in diporphyrins III and IV are coupled with $\mathbf{B}_y$ in porphyrin I, with $\mathbf{B}_x$ in porphyrin VII, and weakly with $\mathbf{B}_x$ in porphyrin V and $\mathbf{B}_y$ in porphyrin VI.

is introduced. The Soret band splitting in the *meso*−*meso*-linked zinc(II) diporphyrin is explained by simple excitonic dipole coupling between zinc(II) porphyrin monomers.[18c,23] In the case of **B*n***, however, more complicated Soret band splittings are expected, because various dipole−dipole excitonic interactions are possible among eight mutually perpendicular porphyrin units (Scheme 2, right). Among sixteen possible exciton coupling states of **B*n***, only two states are transition-allowed (Supporting Information).[31] The low-energy Soret state indicates excitonic dipole−dipole interaction among eight parallel transition dipole moments along the *z*-axis (blue arrows in Scheme 2, right), whereas the high-energy Soret state implies excitonic dipole−dipole interaction among four parallel transition dipole moments along the *x*- or *y*-axis (red or green arrows in Scheme 2, right).[31] Using the reported transition dipole strength (9.5 ± 0.5 D)[32] of the Soret band of the pyridyl-substituted zinc(II) porphyrin monomer (5-(4-pyridyl)triphenylporphyrin) and the porphyrin center-to-center distances (8 × 8 × 10 Å^3), the excitonic Soret band splitting energy ΔE_{Soret} of **B1** was calculated to be ∼1112 cm^{-1}, in good agreement with the experimental splitting value of 1129 cm^{-1} (Supporting Information).[31,33]

The blue shift in the low-energy Soret band of **B1** is due to H-type dipole coupling between molecule I and molecules IV, V, and VIII (Scheme 2, right). The H-type dipole coupling, however, is expected to decrease in going from **B1** to **B2** and **B3**, resulting in the small blue shift of the low-energy Soret band. The excitonic Soret band splitting energies ΔE_{Soret} of **B2** and **B3** were calculated by procedures similar to those used to calculate ΔE_{Soret} of **B1**, in which the different geometrical parameters (8 × 14 × 14 Å^3 for **B2** and 8 × 18 × 18 Å^3 for **B3**) give rise to ΔE_{Soret} values of ∼1635 and ∼1741 cm^{-1} for **B2** and **B3**, respectively, which are larger than ∼1112 cm^{-1} of **B1**. The corresponding experimental values are 1406 and 1540 cm^{-1}, obtained from Table 1. The differences between the calculated values and the experimental ones may be rationalized in terms of plausible conformational flexibilities in larger porphyrin boxes.

The exciton−exciton annihilation, which depends on laser power, has provided rich information about the excitation energy migration processes within the natural light-harvesting antennae of LH1 and LH2, in which the exciton−exciton annihilation was understood in terms of formation of a doubly excited state as a consequence of a Förster-type incoherent energy-transfer process upon the absorption of more than two photons in a single molecular entity. The doubly excited state formed quickly relaxes to the singly excited state.[25,26] Consequently, the observed exciton−exciton annihilation process of **B*n*** is direct evidence of the Förster-type incoherent energy hopping process among many orthogonally associated zinc(II) diporphyrins. It is noteworthy that the two fast annihilation components τ_1 and τ_2 are observed in **B*n***, and the contribution of the latter is more sensitive to the laser power (see the relative amplitudes in Table 3). It is well-known that the energy hopping process is a migration-limited process rather than a trapping-limited process, and the slowest exciton−exciton annihilation component describes well the Förster-type incoherent energy hopping process over a multichromopore system.[25,26]

We have confirmed the excitation energy migration processes within **B*n***, using the exciton−exciton annihilation and anisotropy depolarization. Nevertheless, neither annihilation nor depolarization time represents the straightforward energy hopping times. To obtain the energy hopping times, a modeling of energy migration and the simultaneous consideration of two observables are necessary. The description of the exciton−exciton annihilation and anisotropy depolarization has been well developed for LH1 and LH2, which have cyclic multiporphyrin structures.[23,24,32] In LH1 and LH2, an explicit Förster-type incoherent energy hopping model has been constructed assuming a migration-limited character of exciton−exciton annihilation, and a random walk formalism of anisotropy. In this context, the analytical depolarization and exciton−exciton annihilation times are connected with the excitation energy hopping time by the following equations:[25]

$$\tau_{\text{depolarization}} = \frac{\tau_{\text{hopping}}}{4(1 - \cos^2(2\pi/N))} = \frac{\tau_{\text{hopping}}}{4(1 - \cos^2 \alpha)} \quad (1)$$

$$\tau_{\text{annihilation}} = \frac{N^2 - 1}{24}\tau_{\text{hopping}} \quad (2)$$

where N is the number of hopping sites and α the angle between adjacent transition dipoles (Scheme 4, left). The number of hopping sites N is defined by N_m/L, where N_m is the number of molecules and L the exciton coherence length of the array.[26] The $\tau_{\text{annihilation}}$ value in eq 2 is also defined as the slowest exciton−exciton annihilation time assuming a migration-limited character of the excitons.[26]

Now, we model the excitation energy migration process within **B*n***, and simultaneously use the two different observables to estimate the energy hopping times. The **B*n*** boxes are regarded as a cyclic multiporphyrin array that consists of four mutually perpendicular *meso*−*meso*-linked zinc(II) diporphyrins. They have eight mutually perpendicular porphyrin units; however, the number of hopping sites is $N = 4$, because the hopping sites are four *meso*−*meso*-linked zinc(II) diporphyrins that have an exciton coherence length of $L = 2$ (Scheme 4, right). Although the exciton coherence length of the orthogonally linked zinc(II) porphyrin array is known to be $L \approx 4-5$,[9a,18c] **B*n*** has an exciton coherence length of $L = 2$, because of their noncovalent linkages. To describe the random walk of the anisotropy, the orientations of the molecular transition dipoles

(31) Hwang, I.-W.; Cho, H. S.; Jeong, D. H.; Kim, D.; Tsuda, A.; Nakamura, T.; Osuka, A. *J. Phys. Chem. B* **2003**, *107*, 9977.
(32) Yatskou, M. M.; Koehorst, R. B. M.; Donker, H.; Schaafsma, T. J. *J. Phys. Chem. A* **2001**, *105*, 11425.
(33) (a) Kasha, M. *Radiat. Res.* **1963**, *20*, 55. (b) Kasha, M.; Rawls, H. R.; El-Bayoumi, M. A. *Pure Appl. Chem.* **1965**, *11*, 371. (c) Scholes, G. D.; Ghiggino, K. P. *J. Phys. Chem.* **1994**, *98*, 4580.

Scheme 4. Energy Hopping Model of **B*n***

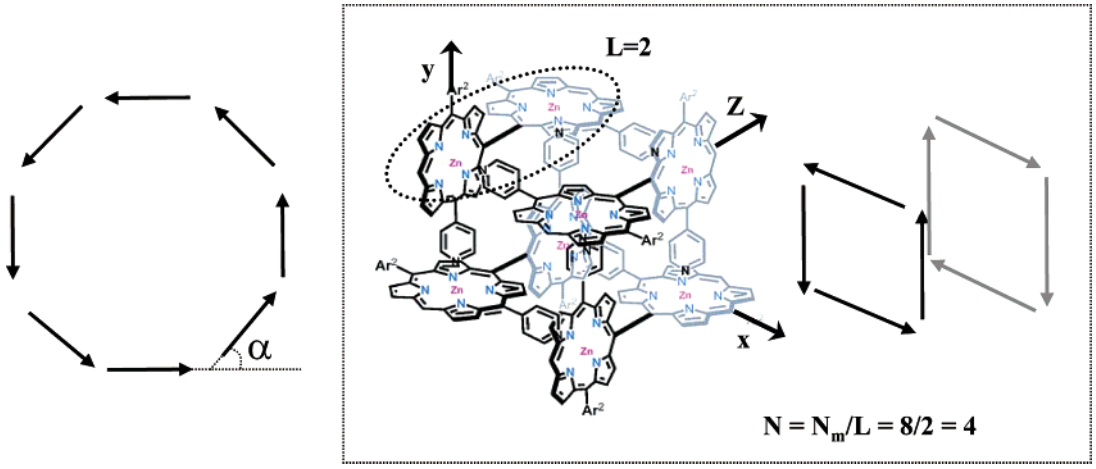

are considered. As shown in Scheme 4, right, the transition dipoles that are attributable to the change of anisotropy are arranged in a rectangular cycle on the *xy*-plane; the energy hopping process among the transition dipoles along the *z*-axis does not change the anisotropy. Consequently, the anisotropy decay profile of **B*n*** reflects the energy hopping process in a forward (black) or backward (gray) rectangular cycle that consists of four mutually perpendicular transition dipole moments. This modeling indicates that the excitation energy migration process within **B*n*** can directly be described by eqs 1 and 2. Introducing $\alpha = 90°$ and $N = 4$, the relations $\tau_{hopping} = 4\tau_{depolarization}$ and $\tau_{hopping} = 1.6\tau_{annihilation}$ are obtained for the **B*n*** boxes. As a consequence, the energy hopping times are calculated to be 48, 100, and 356 ps in **B1**, **B2**, and **B3** using the anisotropy rise times, i.e., $\tau_r = 12$, 25, and 89 ps, given in Figure 5. In a different approach, the energy hopping times are estimated to be 48, 96, and 365 ps using the slowest exciton−exciton annihilation components, i.e., $\tau_2 = 30$, 60, and 228 ps, listed in Table 3. It is noteworthy that the two different observables, exciton−exciton annihilation and anisotropy depolarization, result in consistent excitation energy hopping times within error ranges (48 ps in **B1**, 98 ± 3 ps in **B2**, and 361 ± 6 ps in **B3**). This implies that the excitation energy migration process within **B*n*** is well described by the Förster-type incoherent energy hopping model, because of their well-defined and perpendicular orientations. The calculated energy hopping times of **B*n*** are also well expressed as a function of the distance between adjacent *meso*−*meso*-linked zinc(II) diporphyrins within **B*n***, i.e., $\tau_{EET} \propto R_{DA}^6$ (Figure 6). Finally, using the modeling, the anisotropy rise profiles of **B*n*** that converge to ~0.1 can be understood. Although the coherent energy hopping process within the *meso*−*meso*-linked zinc(II) diporphyrins results in $r_\infty \approx 0$, the energy migration process over the rectangular cycle on the *xy*-plane can give rise to $r_\infty \approx 0.1$, because this process proceeds among the transition dipoles of zinc(II) porphyrin monomers. Similarly, the excitation energy hopping process among the porphyrin monomers within LH1 and LH2 results in $r_\infty \approx 0.1$.[25,34,35]

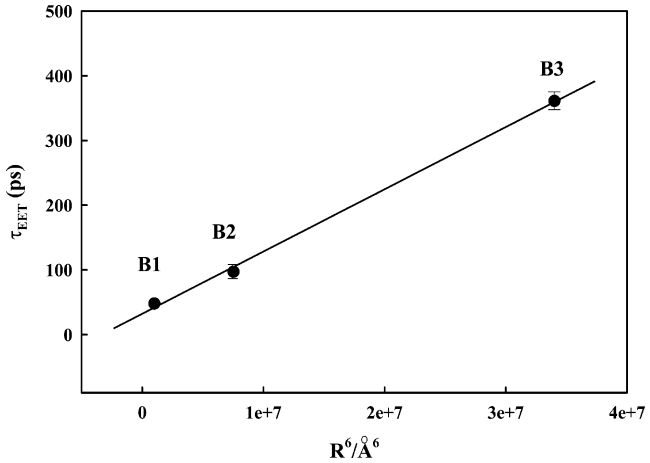

Figure 6. Energy hopping time (τ_{EET}) of **B*n*** as a function of R_{DA}^6.

Conclusions

In noncoordinating solvent, **M*n*** and **D*n*** assemble to form their tetrameric assemblies **S*n*** and **B*n***, respectively. The association constants of **B*n*** are much larger than those of **S*n*** owing to double eight-point simultaneous coordinative interactions. **B*n*** are formed by a homochiral self-sorting assembly process, which has been proved by the optical separation of **B1** and **B2**. The features of exciton coupling within **B*n*** have been revealed by the examinations of the absorption spectra of **B*n*** and the CD spectra of the optically pure **B1** and **B2**. The porphyrin boxes **B*n*** consist of four regularly arranged *meso*−*meso*-linked zinc(II) diporphyrin subunits, which is favorable for a model of light-harvesting antennae. In this regard, we have investigated the excitation energy migration process within **B*n***. The relatively small polarization anisotropy in the steady-state fluorescence excitation spectra and the small initial anisotropy value in the time-resolved fluorescence anisotropy decay reflect the efficient excitation energy hopping processes. Both the exciton−exciton annihilation and the anisotropy rise in femtosecond transient absorption and transient absorption anisotropy describe well the different excitation energy hopping rates within **B*n***. Modeling of the energy migration process within **B*n*** with $N = 4$ and $L = 2$ consistently gave excitation energy hopping times of 48, 98 ± 3, and 361 ± 6 ps among the *meso*−*meso*-linked zinc(II) diporphyrins for **B1**, **B2**, and **B3**, respectively. These results indicate that the excitation energy migration

(34) Jimenez, R.; Dikshit, S. N.; Bradforth, S. E.; Fleming, G. R. *J. Phys. Chem.* **1996**, *100*, 6825.
(35) Chachisvilis, M.; Kühn, O.; Pullerits, T.; Sundström, V. *J. Phys. Chem. B* **1997**, *101*, 7275.

processes within **B*n*** are well described by the Förster-type incoherent energy hopping model, because of their well-defined arrangements and perpendicular orientations. Overall, the porphyrin boxes **B*n*** are demonstrated to serve as a well-defined light-harvesting model exhibiting excitation energy hopping rates that depend on the vertical distance between the *meso*−*meso*-linked zinc(II) diporphyrin subunits.

Experimental Section

Steady-State Spectra. Solutions of the **D*n*** diporphyrins were prepared in approximately micromolar concentrations in pyridine and CH_2Cl_2 solvents. All the solvents (~99.9% purity) were purchased from Merck Chemical Co. (HPLC grade). Absorption spectra were obtained with a Shimadzu model 1601 UV spectrometer, and steady-state fluorescence and excitation spectra were measured by a Hitachi model F-4500 fluorescence spectrophotometer at room temperature. The fluorescence quantum yield was obtained in comparison to the fluorescence quantum yield of ~1.0 of a Rhodamine 101 standard in ethanol at room temperature.

Time-Resolved Fluorescence Decay. A picosecond time-resolved TCSPC system was used for the fluorescence decay and fluorescence anisotropy decay measurements (Supporting Information).

Transient Absorption and Transient Absorption Anisotropy Decay. A dual-beam femtosecond time-resolved transient absorption spectrometer was employed for TA and TAA measurements (Supporting Information).

Acknowledgment. The work at Yonsei was financially supported by the National Creative Research Initiatives Program of the Ministry of Science and Technology of Korea (D.K.). The work at Kyoto was partly supported by a Grant-in-Aid from the Ministry of Education, Culture, Sports, Science and Technology, Japan, and the 21st Century COE Program Kyoto University Alliance for Chemistry (A.O.). We thank Prof. H. Tamiaki of Ritsumeikan University for his allowance for the CD measurements.

Supporting Information Available: Experimental procedures and characterization of the products. This material is available free of charge via the Internet at http://pubs.acs.org.

JA046241E